SUPPLEMENTARY INFORMATION

Metal-dependent inhibition of amyloid fibril formation: Synergistic effects of cobalt–tannic acid networks

Wenjie Zhang,[a] Andrew J. Christofferson,[b] Quinn A. Besford,[a] Joseph J. Richardson,[a] Junling Guo,[a] Yi Ju,[a] Kristian Kempe,[c] Irene Yarovsky*[b] and Frank Caruso*[a]

[a]ARC Centre of Excellence in Convergent Bio-Nano Science and Technology, and the Department of Chemical Engineering, The University of Melbourne, Parkville, Victoria 3010, Australia

[b]School of Engineering, RMIT University, GPO Box 2476, Melbourne, Victoria 3001, Australia

[c]ARC Centre of Excellence in Convergent Bio-Nano Science and Technology, and Monash Institute of Pharmaceutical Sciences, Monash University, Parkville, Victoria 3052, Australia

*Corresponding authors. E-mail: fcaruso@unimelb.edu.au (F.C.); irene.yarovsky@rmit.edu.au (I.Y.)

Materials

$A\beta_{40}$ peptide (DAEFRHDSGYEVHHQKLVFFAEDVGSNKGAIIGLMVGGVV, purity: 95.96%), $A\beta_{42}$ peptide (DAEFRHDSGYEVHHQKLVFFAEDVGSNKGAIIGLMVGGVVIA, purity: 95.34%), and amylin peptide (KCNTATCATQRLANFLVHSSNNFGAILSSTNVGSNTY, purity: 92.31%) were purchased from GL Biochem (China). Dulbecco's phosphate-buffered saline, Dulbecco's modified Eagle's medium, fetal bovine serum, heat-inactivated horse serum, and penicillin-streptomycin were purchased from Life Technologies (USA). All other chemicals were purchased from Sigma-Aldrich (USA). All chemicals were used without further purification. The pH of the solutions was measured by a Mettler-Toledo MP220 pH meter. The Milli-Q water used in all experiments was obtained from a three-stage Millipore Milli-Q plus 185 purification system (Millipore Corporation, USA) with a resistivity greater than 18.2 MΩ cm. All aqueous solutions were filtered with membranes with pore sizes of 220 nm before use.

Quantum mechanics (QM) calculations

To accurately determine the Co(II) coordination complex geometry, QM calculations were performed using Gaussian 09[1] on a model system of one cobalt(II) coordinated with gallic acid (Co^{II}–GA_2), with the initial geometry based on the X-ray crystal structure of cobalt(II) oxalate.[2] For geometry optimization, the density functional theory (DFT) B3LYP hybrid functional was employed with the 6-311G(d,p) basis set, and the polarizable continuum model was used to assess the effects of water implicitly. Geometry optimizations were performed with and without ligands at the axial positions and with high and low electronic spins. Ligands were initially placed with the most electronegative atom ~2.5 Å from the cobalt. For the coordination of water molecules, water clusters of ~4 Å from the cobalt were taken from molecular dynamics simulations. Binding enthalpy calculations were performed on the optimized structures at the

B3LYP/6-311+G(3df,2p) level of theory, with no implicit solvent. Upon comparison of different DFT functionals, Vargas *et al*. found the B3LYP functional performed reasonably well for high-spin octahedral complexes.[3] B3LYP is generally within 3–5 kcal mol^{-1} of complete active space second-order perturbation theory (CASPT2) calculations, but consistently underestimates binding energies of some metal–ligand interactions.[4] Upon comparison of basis sets, Henson *et al*. found that larger basis sets reduced the calculated binding energies by stabilizing the unbound complexes.[5]

Model preparation for molecular dynamics (MD) simulations

Model structures of tannic acid (TA) were taken from our previous work.[6] Co^{II}–TA_2 complexes were solvated in a cubic water box of 70 × 70 × 70 $Å^3$, with two sodium ions added to maintain net neutral charge. We also modeled Co^{II}–TA_2 dimers in three configurations with an initial minimum heavy atom separation of ~10 Å. These dimer systems were solvated in a cubic water box of 100 × 100 × 100 $Å^3$, with four sodium ions added to maintain net neutral charge.

Initial partial charges for Co and chelating oxygens were taken from the electrostatic potential (ESP) high-spin B3LYP data, as consistent with the current Condensed-phase Optimized Molecular Potentials for Atomistic Simulation studies (COMPASS) force-field parameter development strategy.[7] The partial charge of cobalt was adjusted iteratively until the octahedral coordination of water at the axial positions was observed. The remaining atomic charges were calculated by the charge equilibration method[8] to provide net charges of −4 for Co^{II}–GA_2 and −2 for Co^{II}–TA_2.

To correctly model the planar geometry, each chelating oxygen was assigned a different atom type (i.e., oc1–oc4) based on the generic hydroxyl oxygen atom type, o2h,[9] in the published COMPASS force field. Two angles were defined to reproduce the geometry. Force constants of 500 kcal mol^{-1} $Å^{-2}$ for Co–O bonds and 150 kcal mol^{-1} rad^{-2} for O–Co–O angles

were applied to maintain the QM geometry around Co. For the C–C–O–Co dihedrals, force constants of 5 and 15 kcal mol^{-1} were applied to $k_{\phi 1}$ and $k_{\phi 2}$ in the dihedral term of the force field equation[7] respectively. A new atom type for Co^{II} was created in the present study, co2c, with a Lennard–Jones 9-6 sigma 3.0 Å and epsilon 0.10 kcal mol^{-1}. These values were derived from simulations of a single Co(II) ion in a water box of 40 × 40 × 40 $Å^3$, with the sigma and epsilon values systematically modified to produce a water coordination number of 6 and a Co(II) ion–oxygen distance of ~2.1 Å, in agreement with other ion models[10] as well as experimental studies.[11] Lennard–Jones parameters for the sodium ion in the 9-6 functional form[9] were taken from the INTERFACE force field.[12] Published parameters from the COMPASS force field were applied to all other atoms, with missing angles and dihedrals for non-metal interactions taken from the Polymer Consistent Force Field (PCFF).[13]

Molecular dynamics simulations

For all MD simulations, the open-source MD code Large-scale Atomic/Molecular Massively Parallel Simulator (LAMMPS) was used.[14] Electrostatic interactions beyond a 15.5 Å cutoff were evaluated with the particle–particle particle–mesh (PPPM) summation method with an accuracy of 10^{-5} kcal mol^{-1}, and van der Waals interactions were assessed with an atom-based summation using a 15.5 Å cutoff and tail correction. MD simulations were run in the isothermal-isobaric (NPT) ensemble, using the Nosé–Hoover thermostat and barostat to maintain a temperature of 298 K and a pressure of 1 atm, with a time step of 1 fs and an output frequency of 10 ps. Equilibration was defined as the point where the Co^{II}–TA_2 heavy-atom root-mean-square deviation reached a steady value with a standard deviation of less than 1 Å, which on average occurred within 50 ns of simulation time. All analyses were performed on 10 ns of equilibrated trajectory. Twelve monomer and seven dimer simulations were run. Hydrogen bond statistics were calculated with a maximum donor–acceptor heavy atom

distance of 3.5 Å and a minimum angle of 120°. Self-diffusion coefficients were calculated from mean square displacements in time-averaged 1 ns blocks taken over the entire trajectory using the Einstein relation.[15]

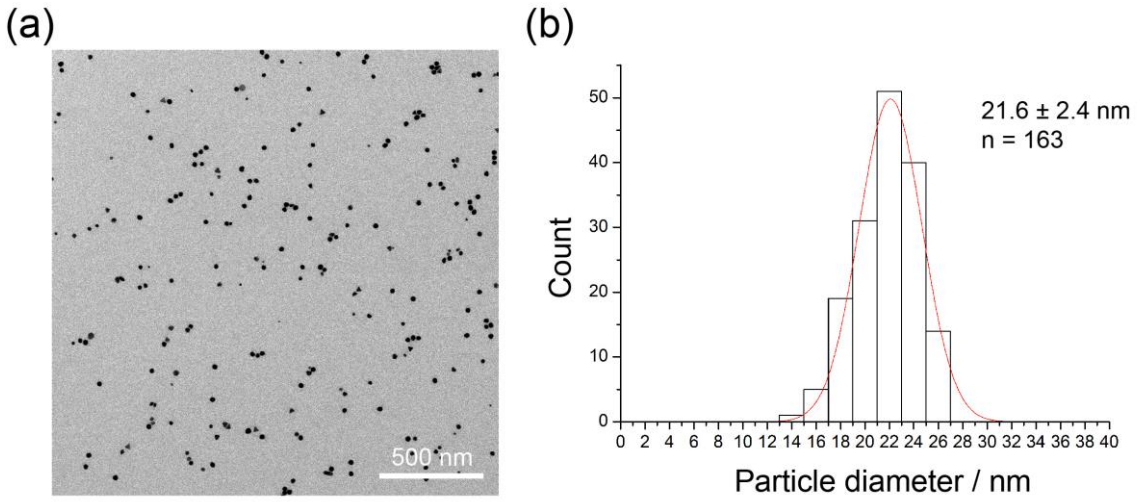

Fig. S1 (a) TEM image and (b) size distribution of TA-AuNPs obtained from a total of 163 particles. Scale bar: 500 nm.

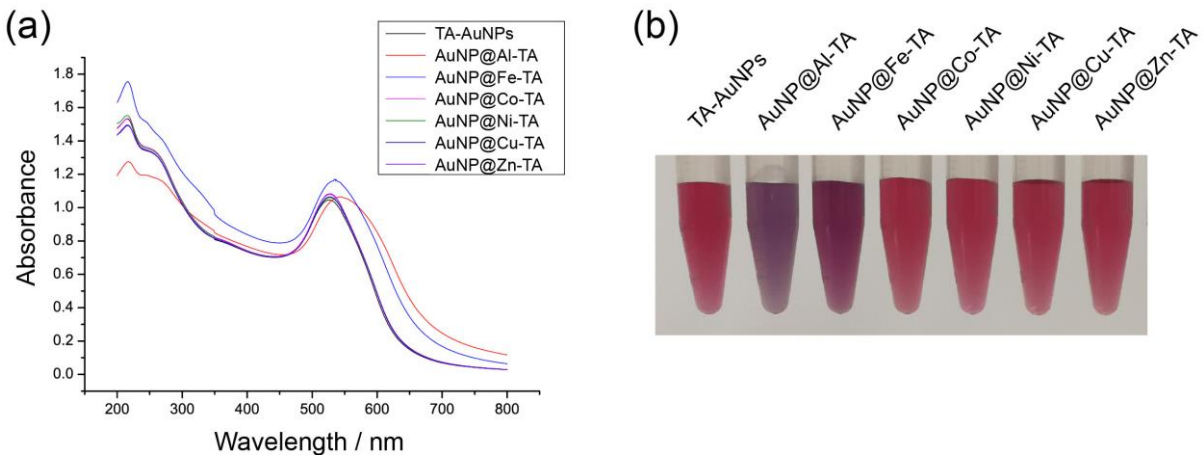

Fig. S2 (a) UV–visible spectra and (b) photograph of pristine TA-AuNPs and MPN-coated AuNPs.

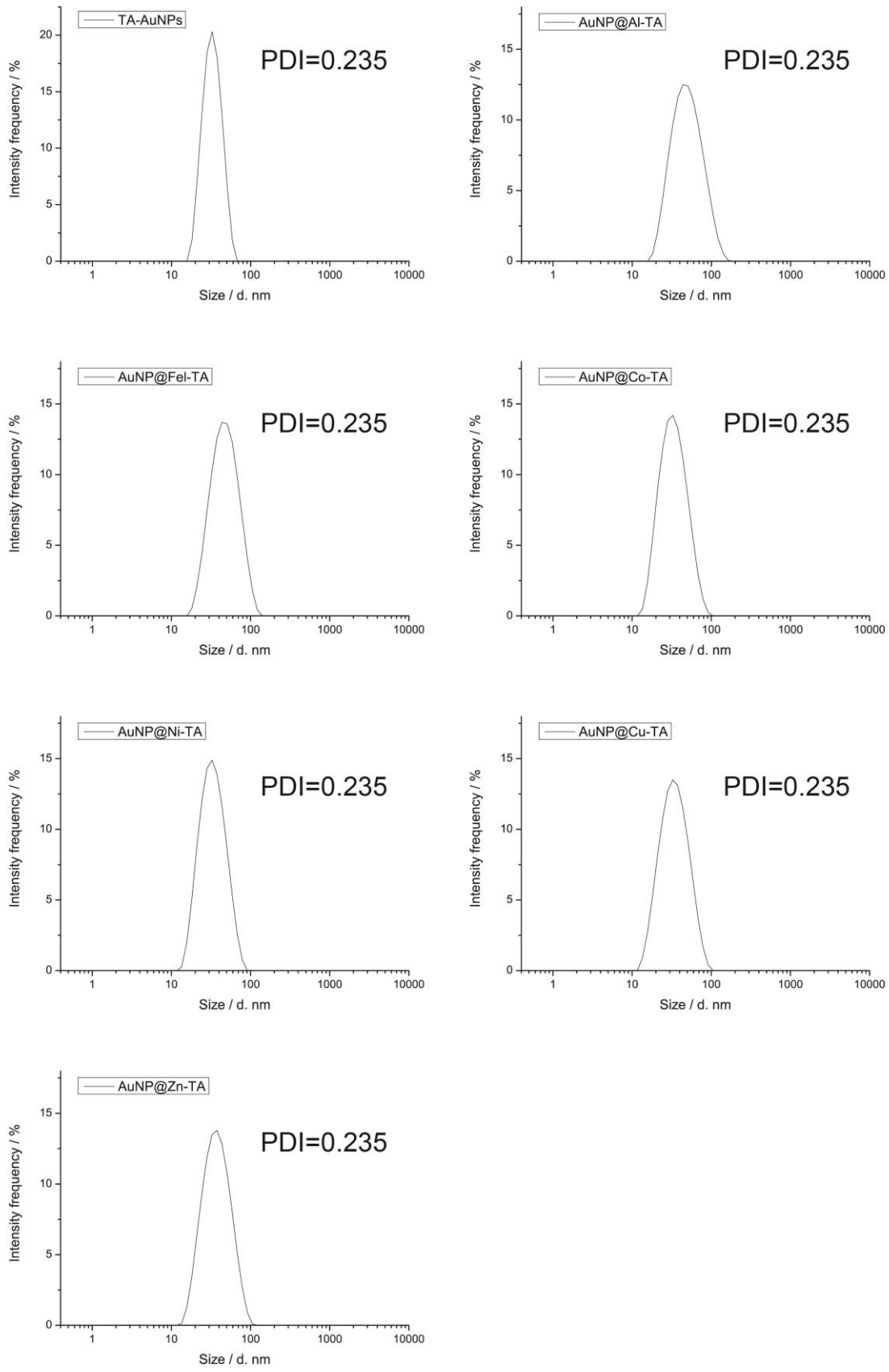

Fig. S3 Size distribution analysis by dynamic light scattering (DLS).

Table S1 Zeta potential and metal concentration of pristine TA-AuNPs and MPN-coated AuNPs.

AuNPs	Zeta potential (mV)	Metal concentration (μM) per nM AuNPs
TA-AuNPs	−33 ± 3	–
AuNP@Al-TA	−38 ± 5	8.2
AuNP@Fe-TA	−38 ± 5	17.7
AuNP@Co-TA	−31 ± 4	1.6
AuNP@Ni-TA	−30 ± 4	2.5
AuNP@Cu-TA	−30 ± 5	11.8
AuNP@Zn-TA	−30 ± 3	8.4

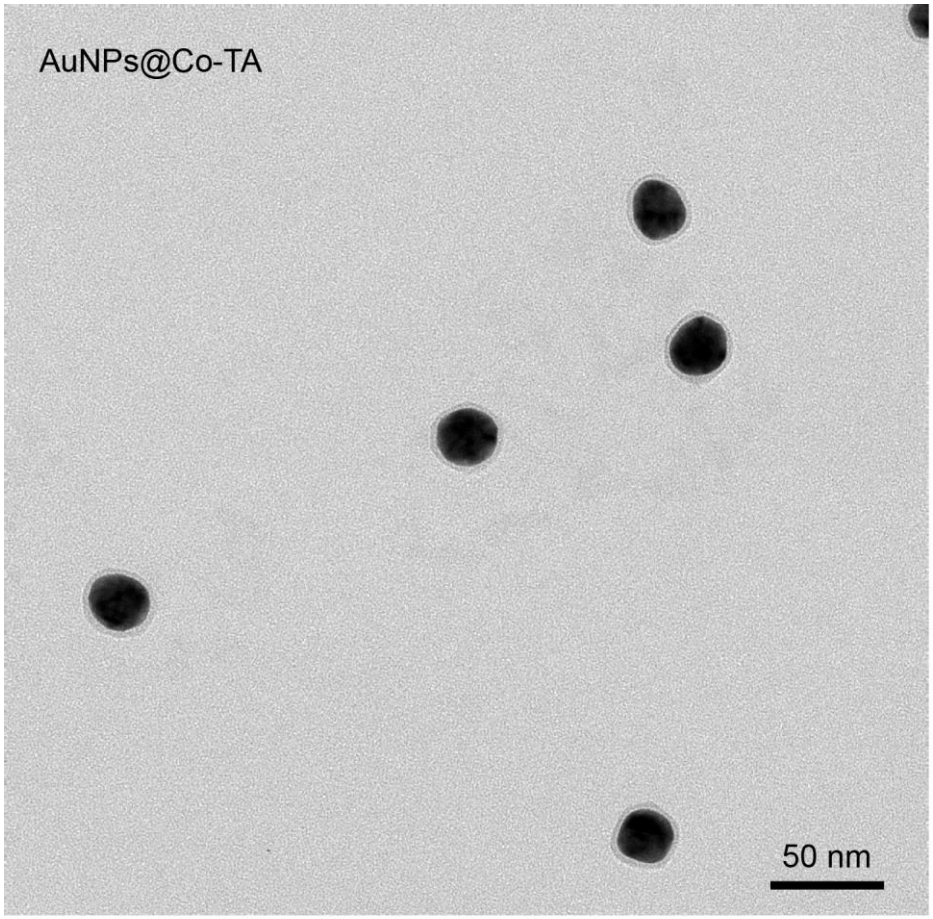

Fig. S4 Transmission electron microscopy (TEM) image of AuNP@Co-TA showing the Co-TA coating.

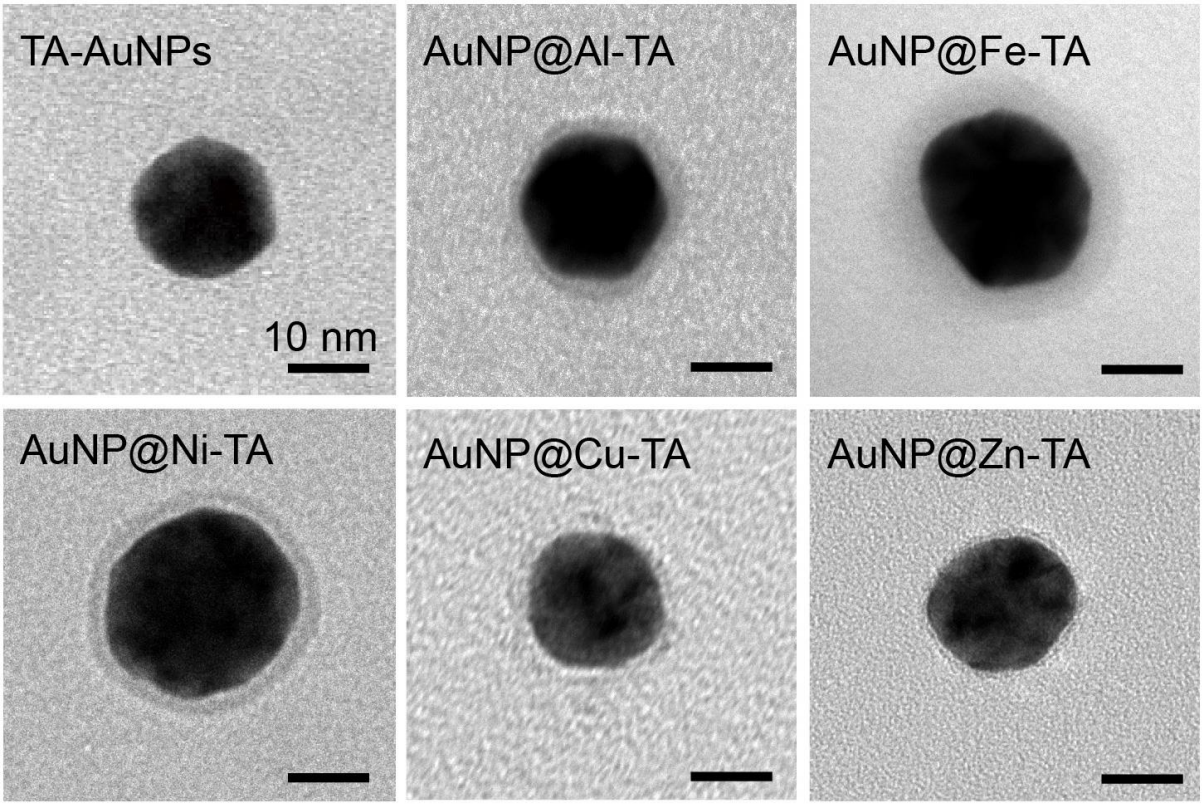

Fig. S5 TEM images of pristine TA-AuNPs and MPN-coated AuNPs. Scale bars: 10 nm.

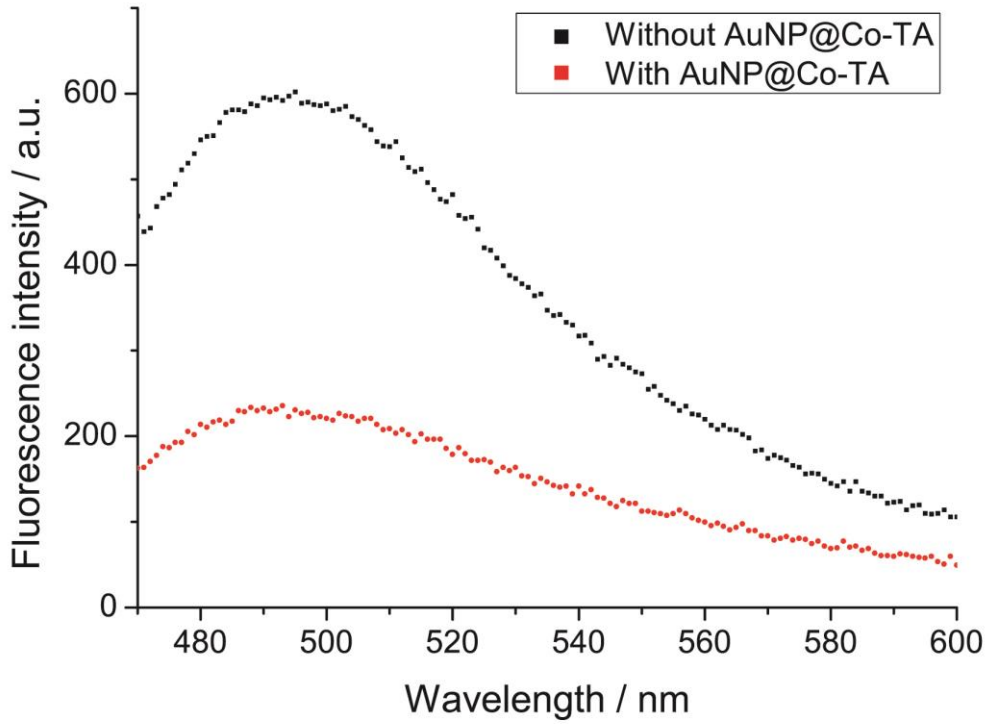

Fig. S6 ThT fluorescence spectra of $A\beta_{40}$ peptides incubated with or without AuNP@Co-TA for 7 days. Excitation wavelength: 440 nm.

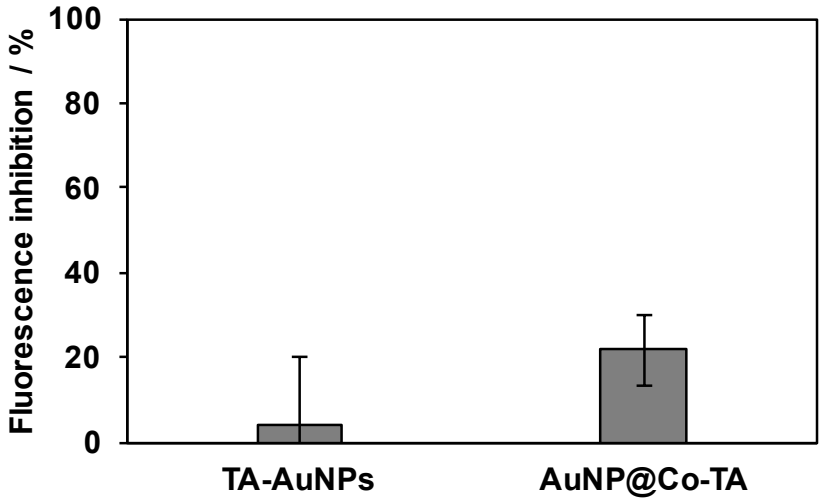

Fig. S7 Inhibition of $A\beta_{42}$ fibril formation based on ThT assay. 10 μM $A\beta_{42}$ peptides were incubated with or without AuNPs for 7 days before measuring the fluorescence intensity of ThT. Data are shown as the mean ± standard deviation (s.d.) of at least three independent experiments.

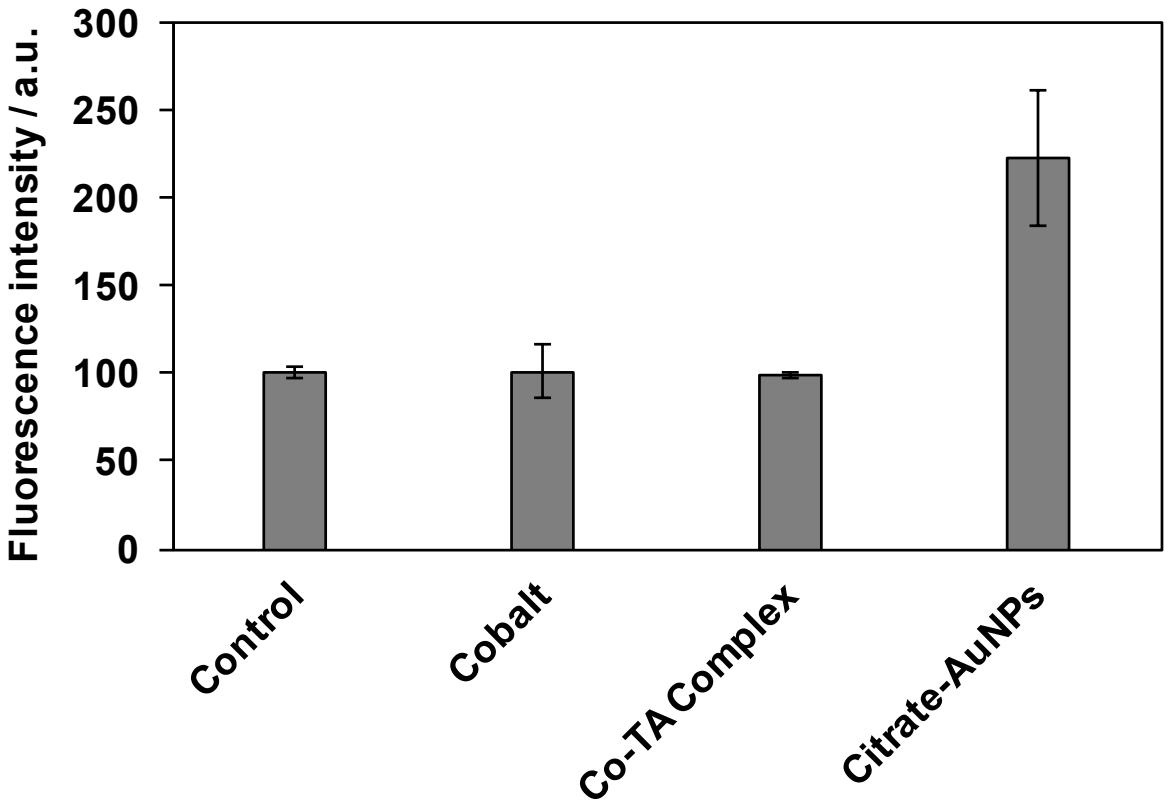

Fig. S8 Effect of free cobalt (Co^{2+}), Co–TA complex, and Citrate-AuNPs on fibril formation of $A\beta_{40}$ peptides. For the study, 10 μM $A\beta_{40}$ peptides were incubated without (Control) or with 0.16 μM Co^{2+}, 0.16 μM Co–TA complex, or 100 pM Citrate-AuNPs for 7 days before measuring the fluorescence intensity of ThT. The ThT fluorescence intensity data shown here were normalized to the fluorescence intensity of the control. Data are shown as the mean ± s.d. of at least three independent experiments.

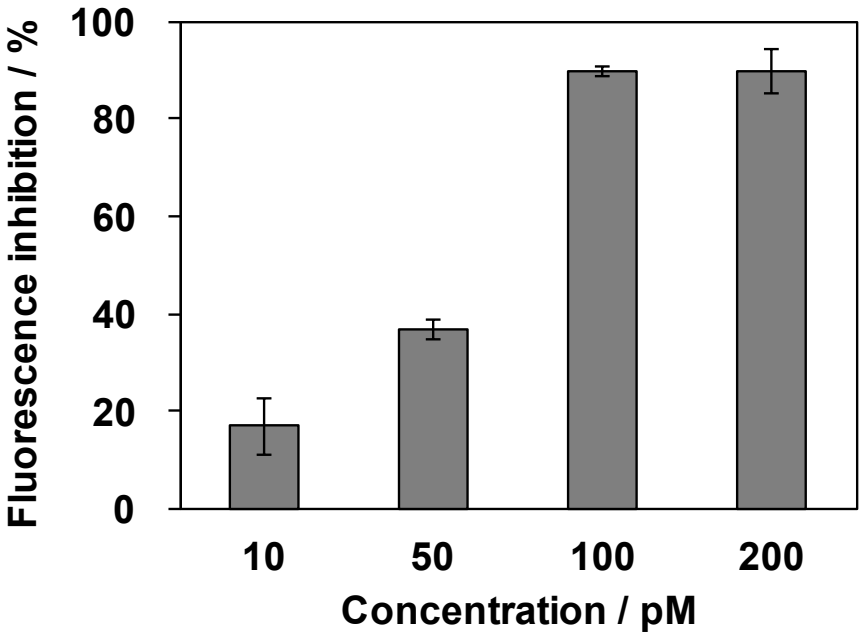

Fig. S9 Fluorescence inhibition as a function of AuNP@Co-TA concentration. Data are shown as the mean ± s.d. of at least three independent experiments.

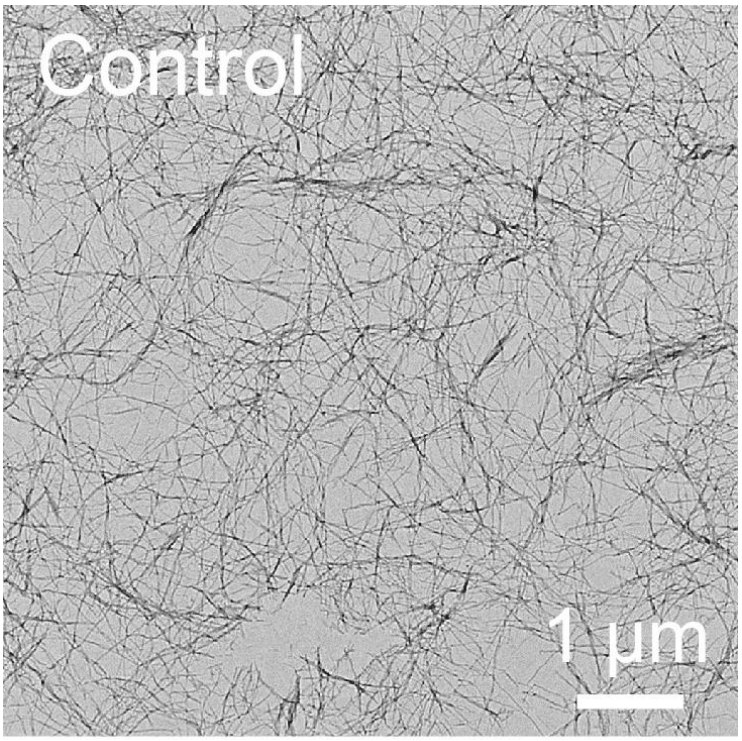

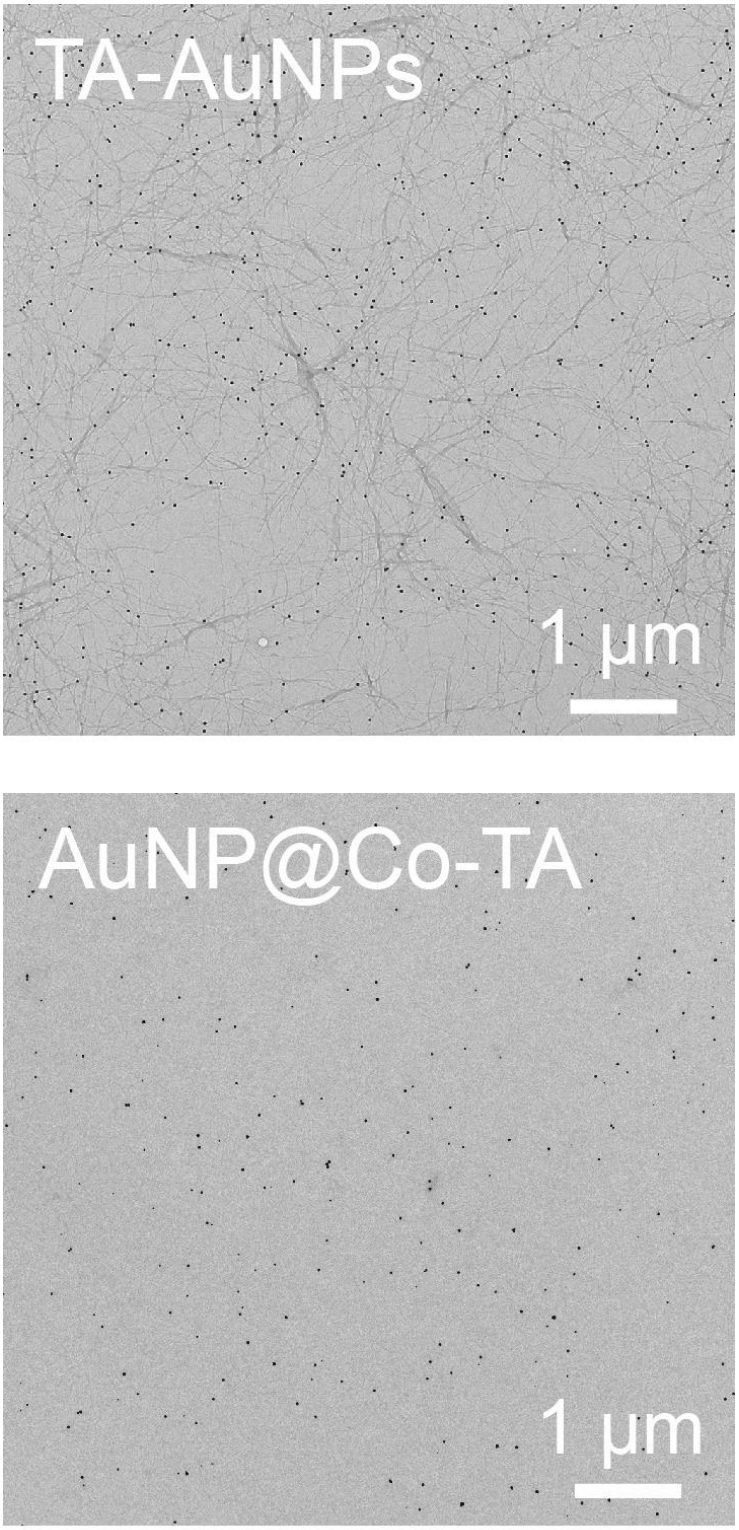

Fig. S10 TEM images of $A\beta_{40}$ peptides incubated in the absence of AuNPs (Control) and in the presence of 100 pM TA-AuNPs or 100 pM AuNP@Co-TA.

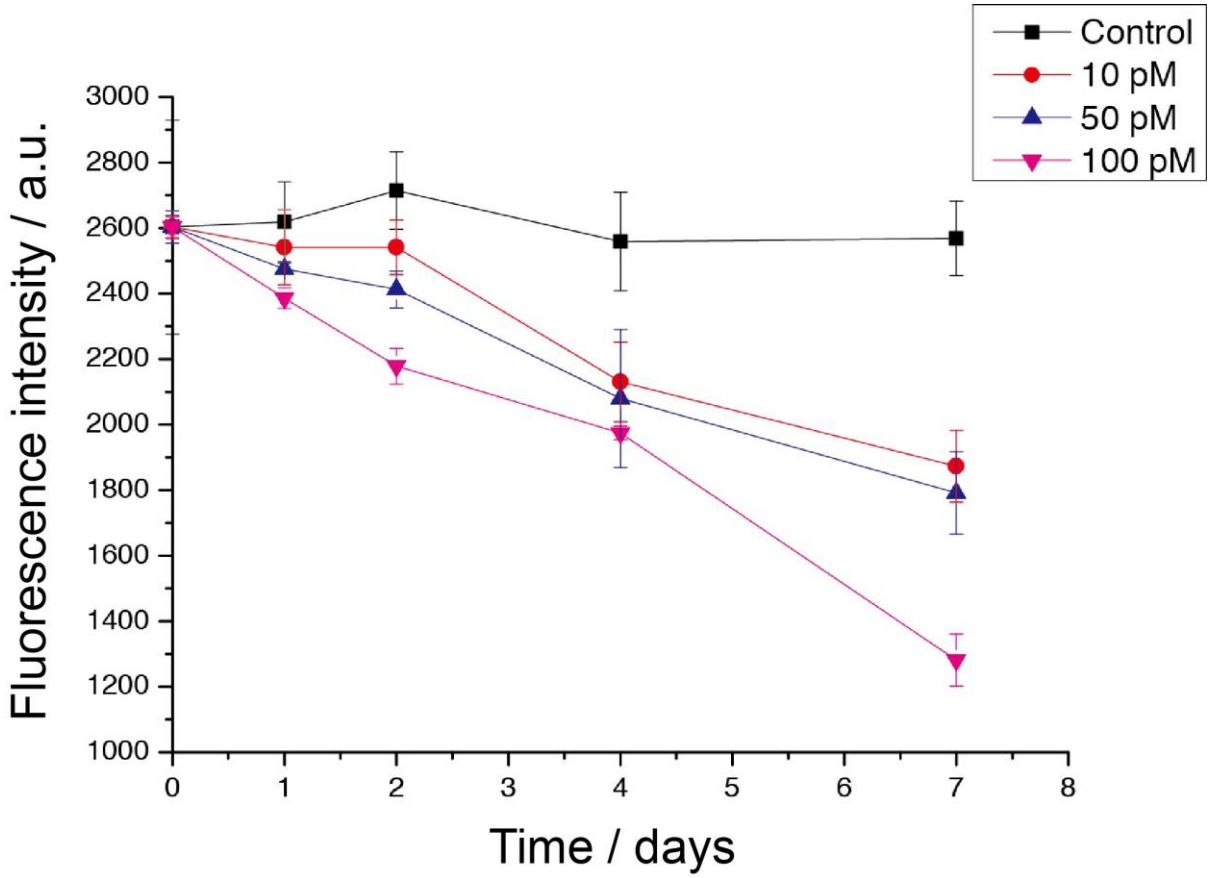

Fig. S11 Disassembly of preformed Aβ$_{40}$ fibrils treated with AuNP@Co-TA at different concentrations. For the formation of the fibrils, 10 μM Aβ$_{40}$ peptides were incubated for 7 days. Data are shown as the mean ± s.d. of at least three independent experiments.

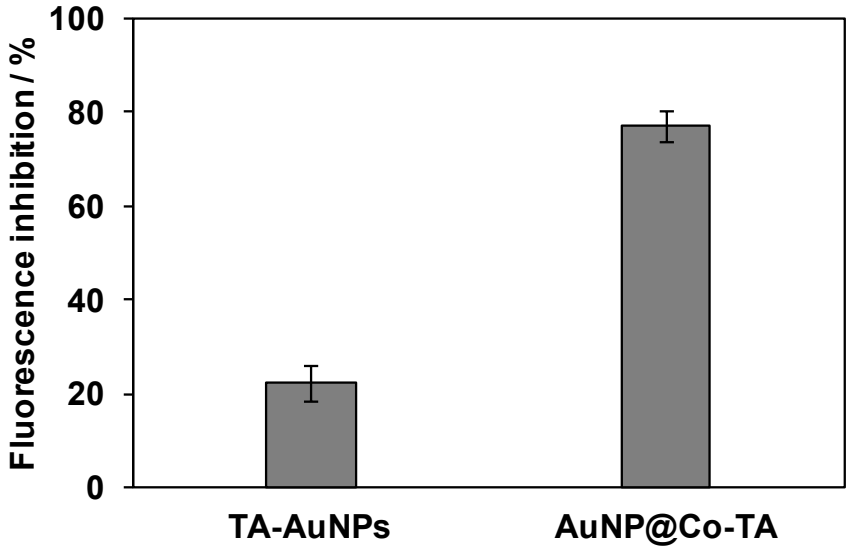

Fig. S12 Inhibition of fibril formation from Aβ$_{40}$ oligomers. Aβ$_{40}$ peptides (10 μM) were incubated alone at 37 °C for 2 h and then kept at 4 °C for 24 h to form oligomers. AuNPs were then added to the solution and the mixture was further incubated at 37 °C for 7 days. Aβ$_{40}$ peptides: 10 μM; AuNPs: 100 pM. Data are shown as the mean ± s.d. of at least three independent experiments.

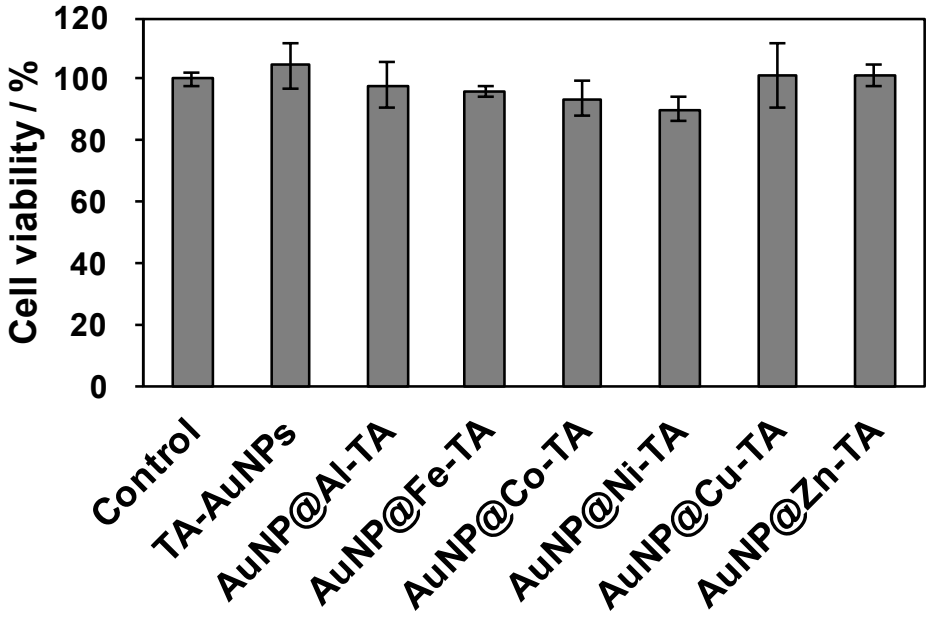

Fig. S13 Cell viability of pristine TA-AuNPs and MPN-coated AuNPs at an AuNP@MPN concentration of 100 pM. PC12 cells were treated with the AuNPs for 48 h before 3-(4,5-dimethylthiazol-2-yl)-2,5-diphenyltetrazolium bromide assay. Control: cells without any treatment. Data are shown as the mean ± s.d. of at least three independent experiments.

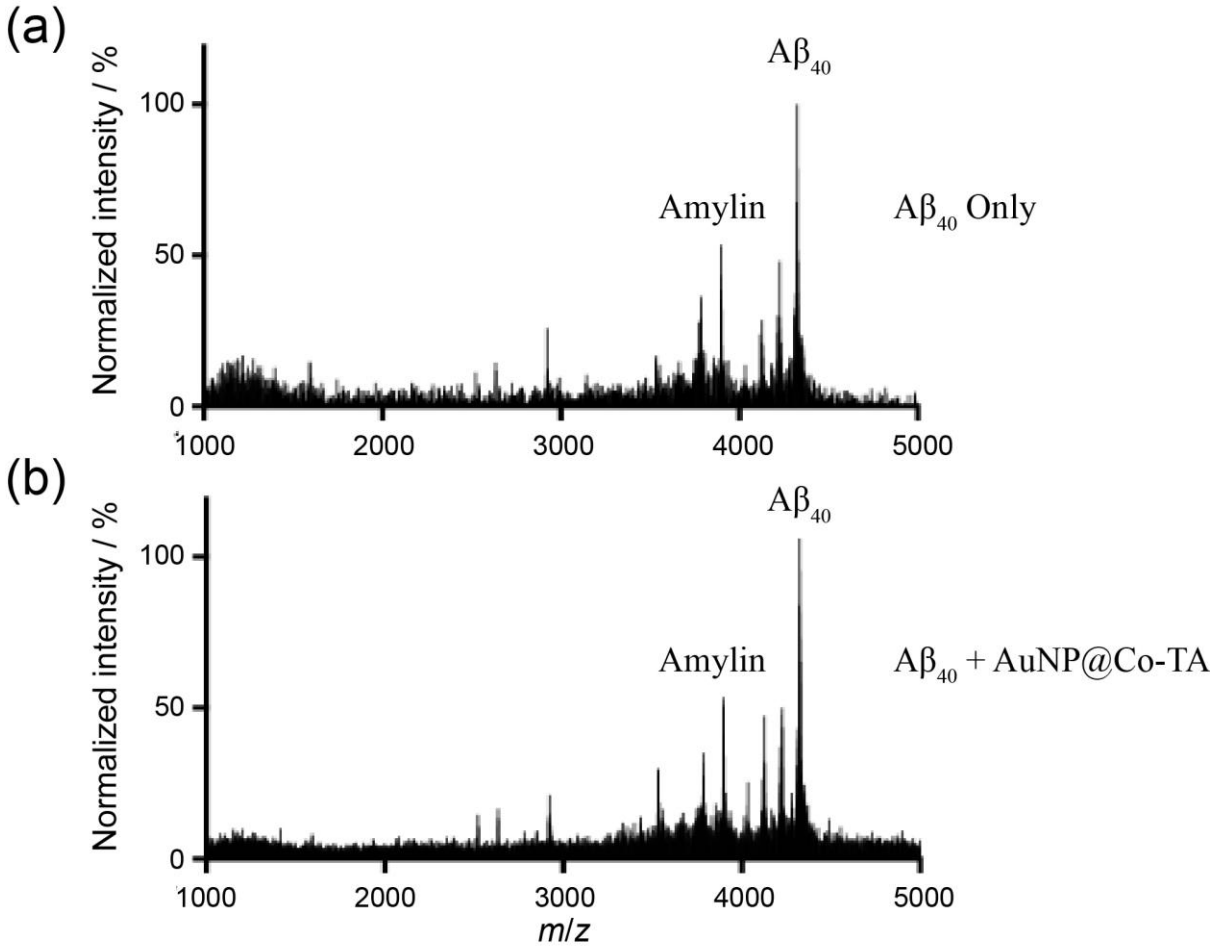

Fig. S14 Matrix-assisted laser deionization/ionization time-of-flight analysis of 100 μM $A\beta_{40}$ treated a) without and b) with 1 nM AuNP@Co-TA after incubation for 7 days. Peptide amylin was used as internal standard.

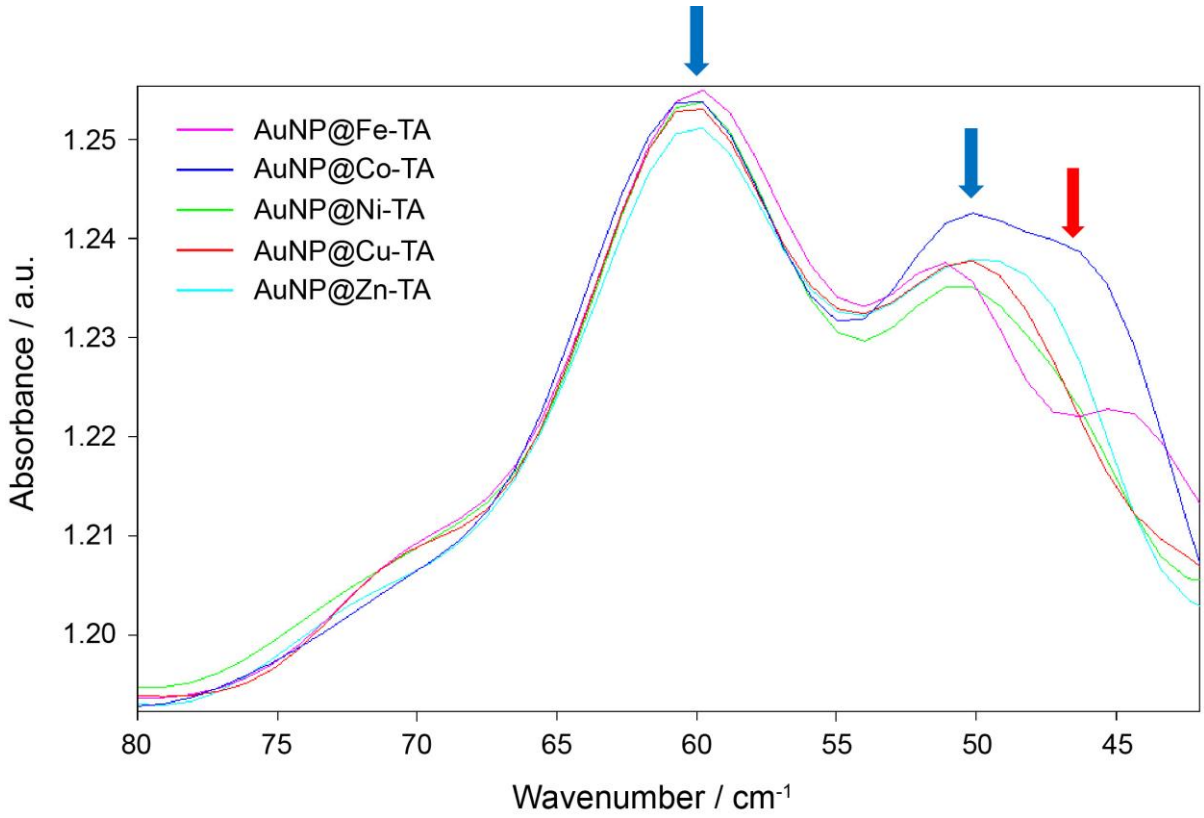

Fig. S15 THz/Far-infrared spectra of different AuNP@MPNs. The blue arrows indicate common peaks for all samples at 60 and 50 cm^{-1}. The red arrow indicates unique peak of AuNP@Co-TA at 46 cm^{-1}.

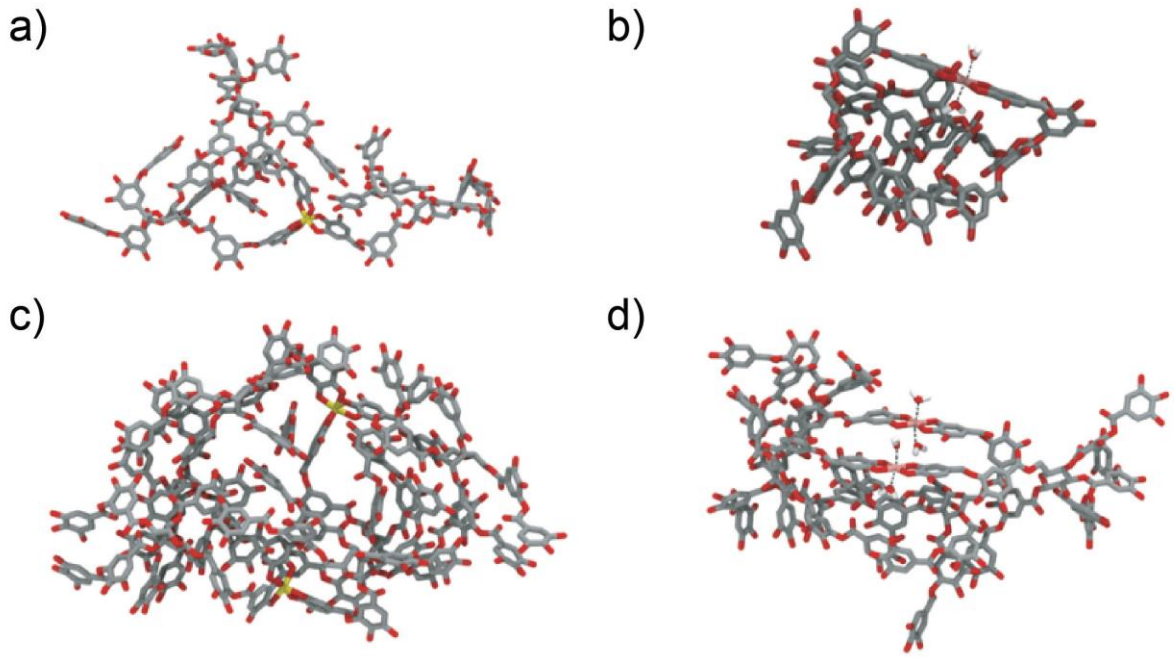

Fig. S16 Representative structures of (a) Fe–TA_3 monomer, (b) Co–TA_2 monomer, (c) Fe–TA_3 dimer, and (d) Co–TA_2 dimer. Iron, cobalt, oxygen, and carbon are colored yellow, pink, red, and silver, respectively. Hydrogens on GA/TA and the solvent molecules are not shown.

Table S2 Cobalt charge models.

Charge Model	Co partial charge[a]	Co-coordinated water exchanges per ns	Co-water contacts (4 Å radius)
1	0.997	0 (no water coordination)	3 ± 1
2	1.600	27.5	3 ± 1
3	1.800	0 (100% occupancy)	3 ± 1

[a]The cobalt partial charge for Charge Model 1 was taken from ESP partial charges from QM calculations of Co–GA_2 at the B3LYP/6-311G* level of theory. The partial charge was then modified by increments of 0.1 until water molecules coordinated at the axial positions of cobalt with 100% occupancy (Charge Model 3). Charge Model 2, with a cobalt partial charge of 1.6, provided the best balance between water coordination and water exchange, with an average water coordination lifetime of 36.4 ps.

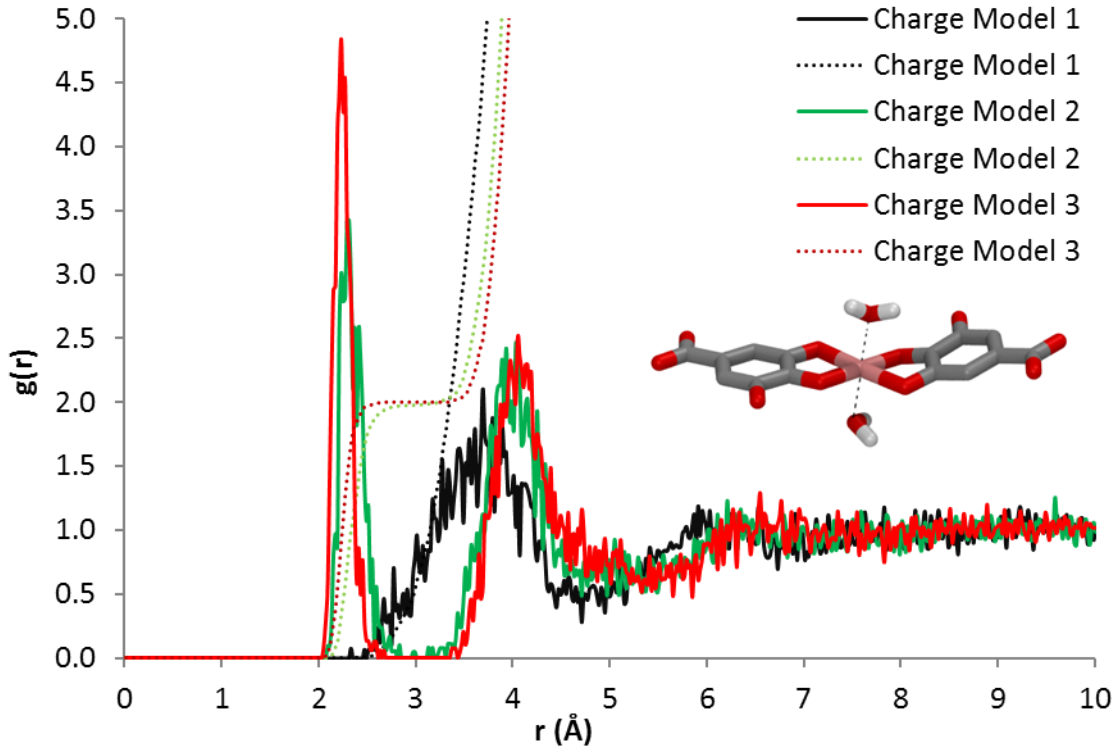

Fig. S17 Radial distribution functions of cobalt–water oxygen for Co^{II}–GA_2 fitted with Charge Model 1 (black), Charge Model 2 (green), and Charge Model 3 (red). The cobalt–water coordination number (the number integral over g(r)) for each Charge Model is shown as a dotted line.

Table S3 Average values for the simulation results obtained for the Co^{II}–TA_2 and Fe^{III}–TA_3 monomer systems.[a]

	Co^{II}–TA_2	Fe^{III}–TA_3
SASA (Å²)	2778 ± 214	3967 ± 275
R_g (Å)	9.3 ± 0.6	13.1 ± 1.4
End-to-end distance (Å)	31 ± 4	47 ± 6
Intramolecular H-bonds	10 ± 5%	10 ± 3%
TA–water H-bonds	141 ± 18%	125 ± 7%
Aromatic ring contacts	9 ± 3	15 ± 3
TA water contacts (4 Å radius)	196 ± 16	281 ± 20
MSD ($\times 10^{-5}$ cm² s^{-1})	0.44 ± 0.04	0.30 ± 0.03

[a]Values for Fe^{III}–TA_3 are taken from our previous work.[6,16] SASA, solvent accessible surface area; R_g, radius of gyration; MSD, mean square displacement.

Table S4 Average values for the simulation results obtained for the Co^{II}–TA_2 and Fe^{III}–TA_3 dimer systems.[a]

	Co^{II}–TA_2	Fe^{III}–TA_3
SASA (Å²)	4974 ± 437	6771 ± 454
Contact area	20 ± 1%	13 ± 3%
R_g (Å)	13.9 ± 1.7	16.4 ± 1.8
End-to-end distance (Å)	50 ± 7	58 ± 7
Intermolecular H-bonds	3 ± 1%	9 ± 2%
TA–water H-bonds	126 ± 8%	116 ± 6%
Aromatic ring contacts	13 ± 5	9 ± 3
TA water contacts (4 Å radius)	353 ± 30	486 ± 32
Metal–metal distance (Å)	13 ± 6	22 ± 6

[a]Values for Fe^{III}–TA_3 are taken from our previous work.[6,16] SASA, solvent accessible surface area; R_g, radius of gyration.

Table S5 Ligand interaction enthalpies and distances for the axial coordination of cobalt in Co^{II}–GA_2.

Ligand[a]	Binding energy (kcal mol^{-1})	Interaction distance (Å)
Water	3.35 (single) 1.44 (1/2)	2.26
Imidazole	−10.93	2.10
Dimethyl sulfide	−5.10	2.51
Acetone	7.52	2.31
Acetate	180	2.24

[a]Methanol, phenol/galloyl, acetamide, hydroxide, and chloride did not coordinate.

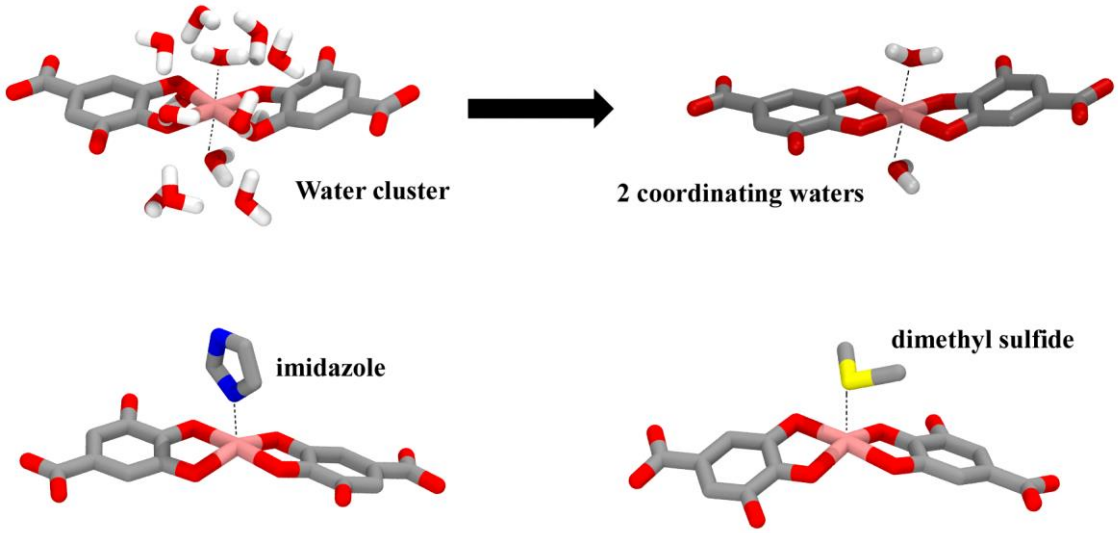

Fig. S18 Optimized structures of amino acid functional groups interacting with Co^{II}–GA_2 at the B3LYP/6-311G* level. Coordinate bonds are shown as black dotted lines. Cobalt, oxygen, sulfur, nitrogen, and carbon are colored pink, red, yellow, blue, and silver, respectively. Hydrogens of Co^{II}–GA_2 and the functional groups are not shown.

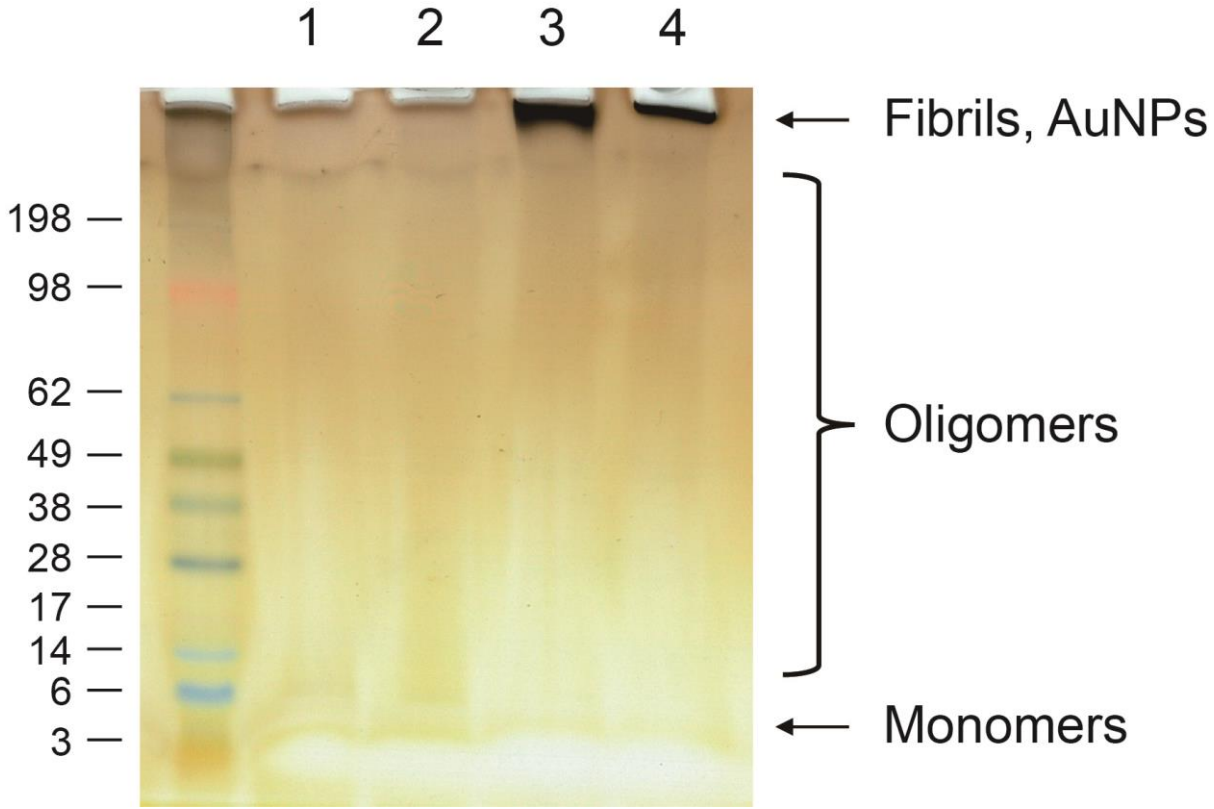

Fig. S19 Analysis of Aβ40 peptides incubated with or without AuNPs by gel electrophoresis with silver staining. Aβ40 peptides: 10 μM; AuNPs: 100 pM. Incubation at 37 °C for 2 days. Lane 1: Aβ40 monomer control; Lane 2: Aβ40 peptides incubated alone; Lane 3: Aβ40 peptides incubated with TA-AuNPs; and Lane 4: Aβ40 peptides incubated with AuNP@Co-TA.

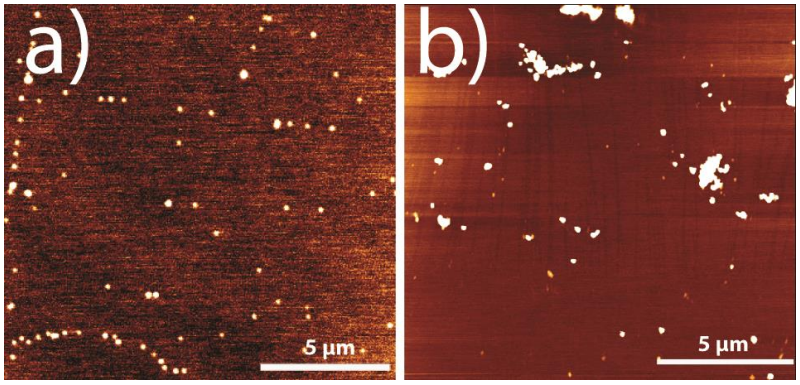

Fig. S20 Analysis of (a) pure AuNP@Co-TA and (b) AuNP@Co-TA incubated with Aβ$_{40}$ peptides by atomic force microscopy. Aβ$_{40}$ peptides: 10 µM; AuNPs: 100 pM. Incubation at 37 °C for 2 days.

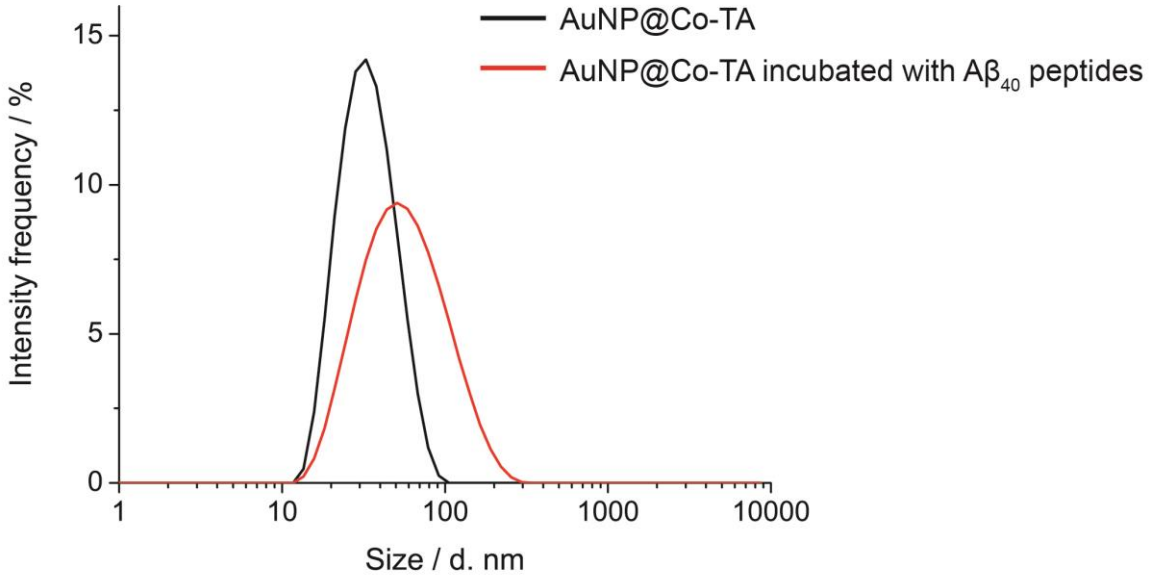

Fig. S21 DLS analysis of AuNP@Co-TA alone and AuNP@Co-TA incubated with Aβ$_{40}$ peptides. Aβ$_{40}$ peptides: 10 µM; AuNPs: 100 pM. Incubation at 37 °C for 2 days. AuNP@Co-TA alone: *Z*-average = 29.00 nm, PDI (polydispersity index) = 0.225; AuNP@Co-TA incubated with Aβ$_{40}$ peptides: *Z*-average = 45.51 nm, PDI = 0.278.

References

1 M. J. Frisch, G. W. Trucks, H. B. Schlegel, G. E. Scuseria, M. A. Robb, J. R. Cheeseman, G. Scalmani, V. Barone, B. Mennucci, G. A. Petersson, H. Nakatsuji, M. Caricato, X. Li, H. P. Hratchian, A. F. Izmaylov, J. Bloino, G. Zheng, J. L. Sonnenberg, M. Hada, M. Ehara, K. Toyota, R. Fukuda, J. Hasegawa, M. Ishida, T. Nakajima, Y. Honda, O. Kitao, H. Nakai, T. Vreven, J. A. Montgomery Jr., J. E. Peralta, F. Ogliaro, M. J. Bearpark, J. Heyd, E. N. Brothers, K. N. Kudin, V. N. Staroverov, R. Kobayashi, J. Normand, K. Raghavachari, A. P. Rendell, J. C. Burant, S. S. Iyengar, J. Tomasi, M. Cossi, N. Rega, N. J. Millam, M. Klene, J. E. Knox, J. B. Cross, V. Bakken, C. Adamo, J. Jaramillo, R. Gomperts, R. E. Stratmann, O. Yazyev, A. J. Austin, R. Cammi, C. Pomelli, J. W. Ochterski, R. L. Martin, K. Morokuma, V. G. Zakrzewski, G. A. Voth, P. Salvador, J. J. Dannenberg, S. Dapprich, A. D. Daniels, Ö. Farkas, J. B. Foresman, J. V. Ortiz, J. Cioslowski and D. J. Fox, Gaussian, Inc., Wallingford, CT, USA, 2009.

2 J. Bacsa, D. Eve and K. R. Dunbar, *Acta Crystallogr. Sect. C Struct. Chem.*, 2005, **61**, m58 – m60.

3 A. Vargas, M. Zerara, E. Krausz, A. Hauser and L. M. Lawson Daku, *J. Chem. Theory Comput.*, 2006, **2**, 1342–1359.

4 P. M. Siegbahn, *J. Biol. Inorg. Chem.*, 2006, **11**, 695–701.

5 N. J. Henson, P. J. Hay and A. Redondo, *Inorg. Chem.*, 1999, **38**, 1618–1626.

6 J. Guo, B. L. Tardy, A. J. Christofferson, Y. Dai, J. J. Richardson, W. Zhu, M. Hu, Y. Ju, J. Cui, R. R. Dagastine, I. Yarovsky and F. Caruso, *Nat. Nanotechnol.*, 2016, **11**, 1105–1111.

7 H. Sun, Z. Jin, C. Yang, R. L. C. Akkermans, S. H. Robertson, N. A. Spenley, S. Miller and S. M. Todd, *J. Mol. Model.*, 2016, **22**, 1–10.

8 A. K. Rappe and W. A. Goddard, *J. Phys. Chem.*, 1991, **95**, 3358–3363.

9 H. Sun, *J. Phys. Chem. B*, 1998, **102**, 7338–7364.

10 P. Li, B. P. Roberts, D. K. Chakravorty and K. M. Merz, *J. Chem. Theory Comput.*, 2013, **9**, 2733–2748.

11 Y. Marcus, *Chem. Rev.*, 1988, **88**, 1475–1498.

12 H. Heinz, T.-J. Lin, R. Kishore Mishra and F. S. Emami, *Langmuir*, 2012, **29**, 1754–1765.

13 H. Sun, S. J. Mumby, J. R. Maple and A. T. Hagler, *J. Am. Chem. Soc.*, 1994, **116**, 2978–2987.

14 S. Plimpton, *J. Comput. Phys.*, 1995, **117**, 1–19.

15 M. P. Allen and D. J. Tildesley, *Computer Simulation of Liquids*, Oxford University Press, New York, 1980.

16 J. Guo, J. J. Richardson, Q. A. Besford, A. J. Christofferson, Y. Dai, C. W. Ong, B. L. Tardy, K. Liang, G. H. Choi, J. Cui, P. J. Yoo, I. Yarovsky and F. Caruso, *Langmuir*, 2017, **33**, 10616–10622.